Research article

Journal of RAMAN SPECTROSCOPY

Received: 21 December 2011 Revised: 27 February 2012 Accepted: 9 March 2012 Published online in Wiley Online Library: 20 July 2012

(wileyonlinelibrary.com) DOI 10.1002/jrs.4078

Identification of oxygen vacancy types from Raman spectra of SnO_2 nanocrystals

L. Z. Liu,[a] T. H. Li,[a,b] X. L. Wu,[a]* J. C. Shen[a] and P. K. Chu[c]

Raman spectra acquired from spherical SnO_2 nanocrystals prepared by pulsed laser ablation and hydrothermal synthesis exhibit three oxygen-vacancy-related Raman modes at 234, 573, and 618 cm^{-1}. The peak location and intensity vary with annealing temperature under O_2 finally approaching those of bulk materials. Density functional calculation discloses that the three Raman modes stem from subbridging, in-plane, and bridging oxygen vacancies, respectively. Raman spectra can thus be used to discern different types of oxygen vacancies in SnO_2 nanocrystals. Copyright © 2012 John Wiley & Sons, Ltd.

Supporting Information may be found in the online version of this article.

Keywords: SnO_2 nanocrystals; Raman spectroscopy; oxygen vacancies; annealing processing; density functional calculation

Introduction

Tin oxide (SnO_2) is one of the attractive functional materials because of potential applications to biophysics, gas sensing, catalysis, and batteries.[1–6] SnO_2 nanostructures with different morphologies such as nanowires (nanorods),[7] nanoribbons (nanobelts),[8,9] and nanocrystals (NCs)[10,11] exhibit some novel characteristics. Because oxygen vacancies (OVs) play a critical role in many of the new physical phenomena,[9,12,13] more accurate identification and better understanding of the different OV structures are of fundamental and technical interest. SnO_2 has a tetragonal rutile structure (space group D_{4h}^{14}, $P42/mnm$) with two molecules per unit cell. The irreducible representation of optic modes is $\Gamma = A_{1g} + A_{2g} + B_{1g} + B_{2g} + E_g + A_{2u} + 2B_{1u} + 3E_u$.[14] The A_{2g} and $2B_{1u}$ modes are neither Raman active nor infrared (IR) active. The symmetrical A_{2u} and E_u modes are IR active, whereas the remaining A_{1g}, B_{1g}, B_{2g}, and E_g modes are Raman active. Raman scattering is a useful tool to identify microstructural changes, and our previous investigations revealed that the Raman mode at ~574 cm^{-1} was closely associated with the in-plane OVs in SnO_2 NCs.[13] The findings suggest that it is possible to correlate the different Raman modes with OV types (bridging and subbridging) and that Raman scattering can be employed to identify the types of OVs and to explore the physical mechanism.

In this work, the Raman spectra acquired from SnO_2 NCs fabricated by pulsed laser ablation are studied systematically. The IR active mode at ~234 cm^{-1} is found to transform into a Raman active mode because of relaxation of the $\boldsymbol{k} = 0$ selection rule induced by subbridging OV. Meanwhile, the existence of bridging OVs downshifts the A_{1g} mode at ~635 to ~618 cm^{-1}. To investigate the underlying mechanism, the density functional theory (DFT) is adopted to derive the Raman spectra of SnO_2 NCs with different OV types, and the results indicate that the 234, 573, and 618 cm^{-1} Raman modes can be used as a fingerprint to identify the types of OVs in SnO_2 nanostructures.

Samples and experiments

Pulsed laser ablation was conducted in water with tin (99.99%) being the target to prepare the SnO_2 NC samples. The detailed experimental setup has been described previously.[15] After drying, the white powders were annealed at temperatures T_a of 400, 600, 800, and 1000 °C for 6 h under both oxygen and vacuum. The preparation conditions of the samples for both pulsed laser ablation and hydrothermal synthesis are listed in Table S1 (Supporting Information) for comparison. The samples were examined by high-resolution transmission electron microscopy (HR-TEM, JEOL-2100) and X-ray diffraction (XRD) (Philips X' Per Pro X-ray diffractometer). The Raman scattering spectra were obtained on a T64000 triple monochromator Raman system with the 514.5-nm line of an argon ion laser as the excitation source without the polarization configuration. The resolution of the spectrometer was 0.5 cm^{-1}. The diameter of the beam spot was 5 μm, and the power on the samples was less than 4 mW to avoid sample degradation due to laser heating.

Results and discussion

The HR-TEM image in Fig. 1(a) depicts the morphology of the SnO_2 NCs in the sample without any post-treatment. They have

* *Correspondence to: Wu, XL, Nanjing National Laboratory of Microstructures and Department of Physics, Nanjing University, Nanjing 210093, China. E-mail: hkxlwu@nju.edu.cn*

a *Nanjing National Laboratory of Microstructures and Department of Physics, Nanjing University, Nanjing 210093, China*

b *College of Electronic Engineering, Guangxi Normal University, Guilin 541004, China*

c *Department of Physics and Materials Science, City University of Hong Kong, Tat Chee Avenue, Kowloon, Hong Kong, China*

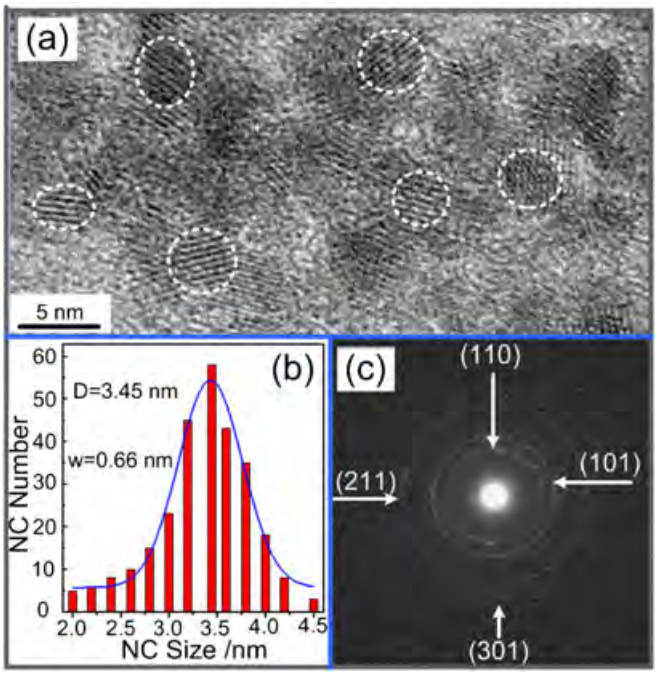

Figure 1. (a) HR-TEM image of the SnO_2 NC sample fabricated by pulsed laser ablation without any post-processing. (b) Size distribution of the SnO_2 NCs calculated from HR-TEM results. (c) SAED pattern of the SnO_2 NCs.

an almost spherical morphology to attain minimum surface free energy. The lattice fringes of 0.343 and 0.265 nm correspond to the (110) and (101) planes of crystalline SnO_2. The Gaussian fit of the SnO_2 NC size distribution is shown in Fig. 1(b) with the probable size and half-width being 3.45 and 0.66 nm. The selected-area electron diffraction (SAED) pattern is displayed in Fig. 1(c), and the three diffraction rings (from inner to outer) are associated with the (110), (101), and (211) planes of rutile SnO_2.

The XRD spectra of the SnO_2 NC samples annealed in O_2 at different T_a are shown in Fig. 2(a). The scan rate of the XRD pattern is 0.25°/s. All the diffraction peaks [(110), (101), and (211)] can be indexed to the crystalline SnO_2 growth planes. As T_a is increased, the diffraction peaks become sharper and stronger indicating that the particles are become bigger and the crystal quality is improved. The Scherrer formula is employed to calculate the average size of the SnO_2 NCs. As T_a is increased, the average sizes increase from 3.5 (the as-made) to 5.5 (400 °C), 6.4 (600 °C), 6.9 (800 °C), and 10.4 nm (1000 °C). Because the XRD patterns acquired from the samples annealed in vacuum are similar to those from the samples annealed in O_2, we infer that the SnO_2 NCs with similar sizes can be obtained in the samples with annealing treatment in vacuum. The Raman spectrum acquired from a SnO_2 NC sample fabricated hydrothermally is also shown in Fig. 2(b) for comparison, and the average size of the NCs is about 3.7 nm as determined by TEM. In addition to the E_u LO mode (S_1) at 353.5 cm^{-1}, E_g mode (S_2) at 430.5 cm^{-1}, and A_{1g} mode (S_4) at 630.0 cm^{-1}, which are related to the small size effect according to Matossi force constant model,[6,16] a strong mode appears at 573.5 cm^{-1} (S3). This mode has been identified to arise from in-plane OVs.[13]

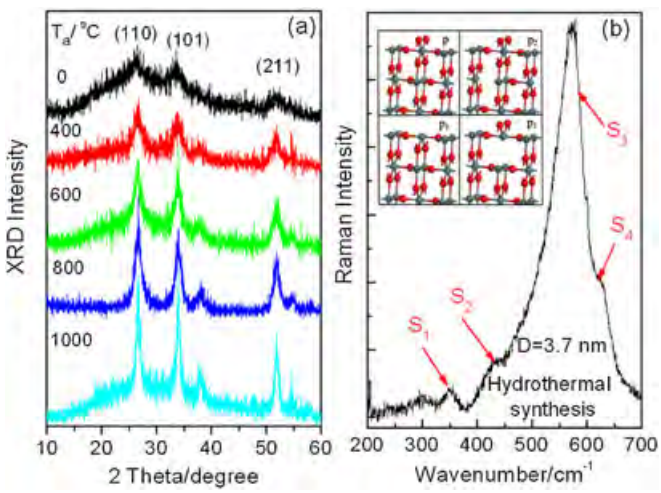

Figure 2. (a) XRD patterns acquired from the SnO_2 NC samples annealed at T_a = 0, 400, 600, 800, and 1000 °C for 6 h under oxygen. (b) Raman spectrum acquired from the spherical SnO_2 NCs with a diameter of 3.7 nm produced hydrothermally. The inset displays the structural schematic diagram used in the DFT calculation for the SnO_2 (110) surface containing different types of OVs – P: without OV; P_1: bridging OV; P_2: in-plane OV; P_3: subbridging OV. Big and small balls represent Sn and O atoms, respectively.

It is known that the types of OVs can be controlled by adopting different fabrication methods and conditions. Here, pulsed laser ablation is utilized to fabricate SnO_2 nanostructures that possibly contain subbridging and bridging OVs. Figure 3(a) shows the representative Raman spectra acquired from the SnO_2 NC samples annealed under oxygen at different T_a. Three weak peaks at 475.5 (f_5), 540.5 (f_3), and 498.5 cm^{-1} (f_2) correspond to the $B_{1u(2)}$, $B_{1u(3)}$, and E_g modes of crystal SnO_2, respectively,[14] and the slight shifts can be attributed to the OV-induced phonon confinement effect. At T_a = 400 °C, the f_4 mode (A_{1g}) wavenumber (at ~619.5 cm^{-1}) and intensity only change slightly compared with those in the unannealed sample, but the intensity of the f_1 mode (E_u TO at ~234.5 cm^{-1}) decreases rapidly. Factor-group analysis indicates that this mode is an IR active mode and it should not appear in the Raman spectrum.[14] However, Abello *et al.*[17] have suggested relaxation of the $\boldsymbol{k} = 0$ selection rule because the perfect crystal is destroyed by the existence of OVs leading the IR to Raman transformation. Die'guez *et al.*[18] have also reported that the SnO_2 nanoparticle surface region is usually covered by a disorder layer containing OVs, and this provides a reasonable explanation of the origin of this mode. At T_a = 600 and 800 °C, the Raman spectra of mode f_1 are only slightly modified, but the mode f_4 wavenumber

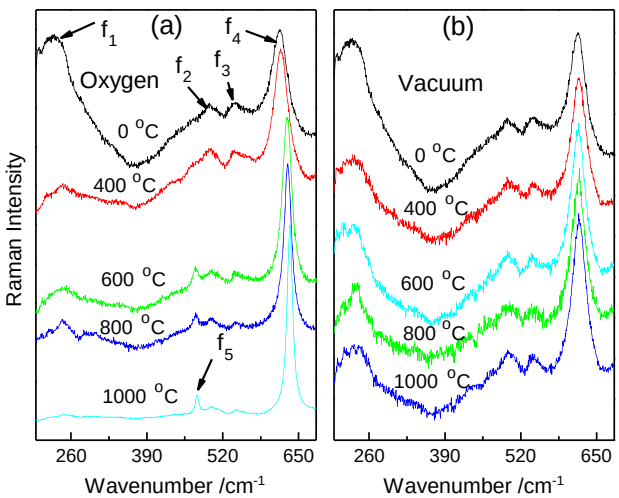

Figure 3. Raman spectra acquired from SnO_2 NC samples annealed at T_a = 0, 400, 600, 800, and 1000 °C under (a) oxygen and (b) vacuum.

Journal of RAMAN SPECTROSCOPY

up-shifts significantly to 631.0 cm^{-1} (bulk) and the intensity is also enhanced. Disappearance of the weak peak (f_1) at $T_a = 1000\,^{\circ}C$ implies that the OVs are finally removed by high-temperature annealing. The results provide evidence that the f_1 and f_4 modes are closely related to OVs.

Campbell and Fauchet's phonon confinement model is used to explain the f_4 mode wavenumber shift.[19,20] When the NC size increases from 5.5 to 10.3 nm, our calculation shows that the wavenumber only shifts from 628.1 to 632.3 cm^{-1}. Therefore, it can be inferred that the size change is not the main reason for the f_4 mode shift. On the basis of the origin of mode f_1, mode f_4 should also be related to the OVs in the NCs. However, an obvious shift in the f_4 mode can be observed at $T_a = 600\,^{\circ}C$, implying that the f_4 mode depends on other types of OVs compared with the f_1 mode. According to the atom displacements model diagram,[14] the physical origins of the f_1 and f_4 modes can be ascribed to the subbridging and bridging OV types, respectively. For confirmation, the samples are also annealed in vacuum, and the corresponding Raman spectra are shown in Fig. 3(b). The Raman spectra are mostly unchanged and the small intensity change can be ascribed to better crystallization. After annealing in vacuum, the sizes of SnO_2 NCs become larger and their surfaces are reconstructed. However, the OV content hardly changes with their morphology transformation.[21] This verifies that OVs play a crucial role in the f_1 and f_4 modes. In addition, a broad shoulder type band appears at ~440–450 cm^{-1} in most of the Raman spectra. The shoulder band may arise from deeper OVs inside SnO_2 NCs. When the sample is annealed in O_2, the NCs grow and the surface OVs vanish easily, but the deeper internal OVs still exist. When the annealing temperature reaches 1000 °C, OVs decrease largely. This leads to the appearance of the shoulder band.[22] For annealing treatment in vacuum, it only makes the SnO_2 NCs grow but does not largely eliminate OVs (especially internal OVs). As a result, the shoulder band hardly changes.

To further explore the origins of the f_1 and f_4 modes, DFT is adopted to calculate the Raman characteristics of SnO_2 structures with different types of OVs along the (110) plane. With the use of the Broyden–Fletcher–Goldfarb–Shanno minimizer in the CASTEP package with default convergence tolerances of 1.0×10^{-5} eV for energy and 0.3 eV/nm for maximum displacement,[9,13,23] the geometric structures of all the supercells are optimized to obtain stable structures as shown in the inset of Fig. 2. In our calculation, the norm-conserving pseudo-potential method is chosen together with the gradient correction and Perdew–Burke–Ernzerhof potential function.[24] The calculated Raman spectra of the SnO_2 structures containing bridging, subbridging, and in-plane OVs as well as without OVs (P_1, P_3, P_2, and P, respectively in the inset of Fig. 2) are presented in Fig. 4(a). In the presence of in-plane OVs, the S_3 mode at ~573.5 cm^{-1} (line b) can be clearly observed. The existence of a bridging OV type (line c) causes the wavenumber of the f_4 mode to downshift, and a weak f_1 mode appears at the same time. Compared with the result of no OV, the subbridging OVs hardly affect the position of mode f_4 but slightly change its intensity. Evidently, the behavior of the f_1, S_3, and f_4 modes is different from that of the sample without OV (line a), and it depends strongly on the OV types. According to the calculated Raman spectra shown in Fig. 4(b), the experimental results can be explained. Firstly, the combined action of subbridging and bridging OVs not only effectively enhances the f_1 mode intensity but also downshifts the wavenumber of mode f_4 (line g), as consistent with the experimental

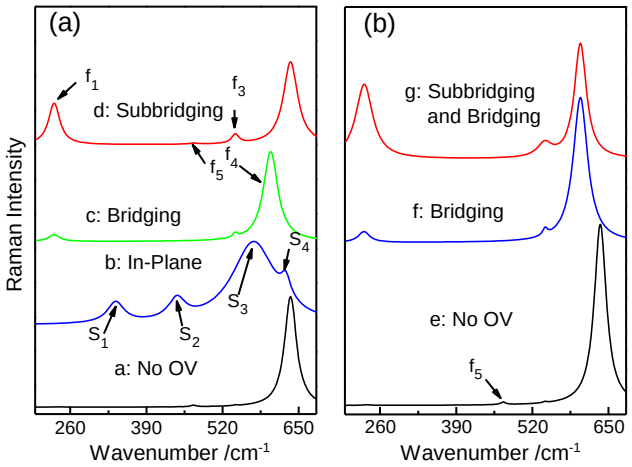

Figure 4. (a) Calculated Raman spectra with different OV types. (b) Calculated Raman spectra for comparison with the corresponding experimental Raman results.

results obtained from the $T_a = 0\,^{\circ}C$ sample in Fig. 3(a). Annealing at $T_a = 400\,^{\circ}C$ eliminates the subbridging OVs on the NC surface. As a result, the intensity of mode f_1 diminishes abruptly, but the wavenumber only up-shifts slightly, whereas the intensity and wavenumber of mode f_4 do not vary. This implies that bridging OVs still exist as verified by the calculated result (line f). Annealing at $T_a = 600\,^{\circ}C$ removes the bridging OVs. Mode f_4, which is affected by the bridging OV, returns to the position of the bulk mode. The residual weak peak at ~245.6 cm^{-1} (f_1) ($T_a = 600$ and 800 °C) may be related to OVs inside the NC. They can be completely eliminated at $T_a = 1000\,^{\circ}C$ and approach those of the calculated Raman spectrum without OVs (line e). The experimental and theoretical results indicate that the subbridging, bridging, and in-plane OVs are responsible for the f_1, f_4, and S_3 modes, respectively. The small deviation between the calculated and experimental data may be due to the complex nature of the samples. In order to read conveniently the peak positions in Figs 2–4, we have listed various peak wavenumbers in Tables S2 and S3 (Supporting Information) for comparison.

Conclusion

In summary, the Raman spectra acquired from spherical SnO_2 NCs produced by pulsed laser ablation show that as the annealing temperature T_a increases, the 234.5 and 618 cm^{-1} modes exhibit reduced intensity and location shift, respectively. Our DFT calculation reveals that the two modes depend strongly on the subbridging and bridging OVs and the 573.5 cm^{-1} mode arises from the in-plane OVs.[13] Our results demonstrate that Raman scattering can be used to identify the types of OVs in SnO_2 nanostructures.

Acknowledgements

This work was jointly supported by Grants (Nos. 2011CB922102 and 60976063) from the National Natural Science Foundation and Basic Research Programs of China, and Postdoctoral Science Foundation of China and Jiangsu Province (Nos. 2011M500889 and 1102001B). Partial support was also from PAPD and Hong Kong Research Grants Council (RGC) General Research Fund (GRF) No. CityU 112510.

Supporting information

Supporting Information may be found in the online version of this article.

References

[1] S. Brovelli, A. Chiodini, A. Lauria, F. Meinardi, A. Paleari, *Phys. Rev. B* **2006**, *73*, 073406.
[2] C. Killic, A. Zunger, *Phys. Rev. Lett.* **2002**, *88*, 095501.
[3] S. O. Kucheyev, T. F. Baumann, P. A. Sterne, Y. M. Wang, T. Buuren, A. V. Hamza, L. J. Terminello, T. M. Willey, *Phys. Rev. B* **2005**, *72*, 035404.
[4] Y. Idota, T. Kubota, A. Matsufuji, Y. Maekawa, T. Miyasaka, *Science* **1997**, *276*, 1395.
[5] R. Asahi, T. Morijawa, T. Ohwaki, K. Aoki, Y. Taga, *Science*, **2001**, *293*, 269.
[6] Y. J. Chen, L. Nie, X. Y. Xue, Y. G. Wang, T. H. Wang, *Appl. Phys. Lett.* **2006**, *88*, 083105.
[7] L. Z. Liu, X. X. Li, X. L. Wu, X. T. Chen, P. K. Chu, *Appl. Phys. Lett.* **2011**, *98*, 133102.
[8] J. Q. Hu, Y. Bando, Q. L. Liu, D. Golberg, *Adv. Funct. Mater.* **2003**, *13*,493.
[9] H. T. Chen, S. J. Xiong, X. L. Wu, J. Zhu, J. C. Shen, P. K. Chu, *Nano Lett.* **2009**, *1926*.
[10] E. J. H. Lee, C. Ribeiro, T. R. Giraldi, E. Longo, E. R. Leite, J. A. Varela, *Appl. Phys. Lett.* **2004**, *84*, 1745.
[11] L. H. Jiang, G. Q. Sun, Z. H. Zhou, S. G. Sun, Q. Wang, S. Y. Yan, H. Q. Li, J. Tian, J. S. Guo, B. Zhou, Q. Xin, *J. Phys. Chem. B* **2005**, *109*, 8774.
[12] M. A. Mäki-Jaskari, T. T. Rantal, *Phys. Rev. B* **2002**, *65*, 245428.
[13] L. Z. Liu, X. L. Wu, F. Gao, J. C. Shen, T. H. Li, P. K. Chu, *Solid State Commun.* **2011**, *151*, 811.
[14] T. Hirata, K. Ishioka, M. Kitajima, H. Doi, *Phys. Rev. B* **1996**, *53*, 8442.
[15] T. H. Li, L. Z. Liu, X. L. Wu, J. C. Shen, F. Gao, P. K. Chu, *Appl. Phys. Lett.* **2010**, *97*, 121901.
[16] J. Zou, C. Y. Xu, X. M. Liu, C. S. Wang, C. Y. Wang, Y. Hu, Y. T. Qian, *J. Appl. Phys.* **1994**, 75, 1835.
[17] L. Abello, B. Bochu, A. Gaskov, S. Koudryavtseva, G. Lucazeau, M. Roumyantseva, *J. Solid State Chem.* **1998**, *135*, 78.
[18] A. Diéguez, A. Romano-Rodríguez, A. Vilà, J. R. Morante, *J. Appl. Phys.* **2001**, *90*, 1550.
[19] L. Z. Liu, X. L. Wu, Z. Y. Zhang, T. H. Li, P. K. Chu, *Appl. Phys. Lett.* **2009**, *95*, 093109.
[20] I. H. Campbell, P. M. Fauchtet, *Solid State Commun.* **1986**, *58*, 739.
[21] T. H. Li, L. Z. Liu, X. X. Li, X. L. Wu, H. T. Chen, P. K. Chu, *Opt. Lett.* **2011**, *36* 4296.
[22] K. N. Yu, Y. H. Xiong, Y. L. Liu, C. S. Xiong, *Phys. Rev. B* **1997**, *55*, 2666.
[23] L. Z. Liu, X. L. Wu, J. C. Shen, T. H. Li, F. Gao, P. K. Chu, *Chem. Comm.* **2010**, *46*, 5539.
[24] B. G. Pfrommer, M. Cote, S. G. Louie, M. L. J. Cohen, *J. Comput. Phys.* **1997**, *131*, 233.

Supporting Information

Identification of Oxygen Vacancy Types from Raman Spectra of SnO_2 Nanocrystals

L. Z. Liu, T. H. Li, X. L. Wu, J. C. Shen, and Paul K. Chu

Table S1. The comparison for preparation conditions between pulsed laser ablation and hydrothermal synthesis methods

Method	Preparation condition
Hydrothermal synthesis	Reactant: $NH_3 \cdot H_2O$ and $SnCl_4 \cdot 5H_2O$ Condition: pH=7 Temperature: 200°C
Pulsed laser ablation	Reactant: Sn target and H_2O Laser power: 250 mJ/pulse Laser wavelength: 248 nm

Table S2. Peak positions in the experimental Raman spectra of Figure 2 and comparison with the calculated results of Figure 4

Peak	Mode	Shift (cm^{-1})	
		Experimental	Calculated
S_1	E_u	353.5	337.7
S_2	E_g	430.5	—
S_3	(In-Plane OV)	573.5	573.5
S_4	A_{1g}	630.0	627.2

The sample is prepared by hydrothermal synthesis method, and peak S_3 originates from in-plane oxygen vacancies.

Table S3. Peak positions in the experimental Raman spectra of Figure 3 at different annealing temperatures, T_a = 0, 400, 600, 800, 1000°C, and comparison with the calculated results of Figure 4

Peak	Mode	Shift (cm^{-1})											
		T_a=0°C		T_a=400°C		T_a=600°C		T_a = 800°C		T_a = 1000°C		Calculated	
		Oxygen	Vacuum	Oxygen	Vacuum	Oxygen	Vacuum	Oxygen	Vacuum	Oxygen	Vacuum	OV	no OV
f_1	E_u	234.5	234.5	245.6	234.5	245.6	234.5	245.6	234.5	—	234.5	232.8	—
f_2	E_g	498.5	498.5	498.5	498.5	499.3	498.5	499.3	498.5	499.3	498.5	—	—
f_3	$B_{1u(3)}$	540.5	540.5	540.5	540.5	540.5	540.5	540.5	540.5	540.5	540.5	543.5	543.5
f_4	A_{1g}	619.5	619.5	619.8	619.5	630.4	619.5	631.2	619.5	633.2	619.5	602.9	627.2
f_5	$B_{1u(2)}$	—	—	—	—	475.5	—	475.5	—	—	475.5	475.5	475.5

The samples are prepared by pulsed laser ablation, and peaks f_1 and f_4 are affected by subbridging and bridging oxygen vacancies, respectively.